Journal of Applied Fluid Mechanics, Vol. 18, No. 5, pp. 1335-1348, 2025.
Available online at www.jafmonline.net, ISSN 1735-3572, EISSN 1735-3645.
https://doi.org/10.47176/jafm.18.5.2970

Study on the Characteristics and Formation Mechanism of Pressure Fluctuation in an Axial Flow Pump Based on Dynamic Mode Decomposition

Z. Y. Zhuang[1], H. H. Zhou[2] and Z. Y. Yu[1†]

[1] *School of Mechanical Engineering, Beijing Institute of Technology, Beijing, 100081, China*
[2] *School of Mechanical Engineering, Hubei University of Automotive Technology, Shiyan, 442000, China*

†*Corresponding Author Email: yuzhiyi@bit.edu.cn*

ABSTRACT

In this study, aiming at investigating the formation mechanism of pressure fluctuations of different frequencies in axial flow pumps, the characteristics of pressure fluctuation were determined using fast Fourier transform (FFT) on the basis of a numerical simulation of complex flow fields in the pump. The pressure and velocity modes corresponding to the primary pressure fluctuation frequency in the pump were decoupled and rebuilt using dynamic mode decomposition (DMD). The consequences showed that the primary pressure fluctuation frequencies in impeller were $11f_n$ and $4f_n$ and in diffuser were $4f_n$ and $2f_n$, respectively, where f_n is the shaft natural frequency. Moreover, the pressure fluctuation amplitude in diffuser was significantly larger than that in the impeller. DMD could identify the coherent structures of various frequency pressure fluctuations in the impeller and diffuser. In addition, the used method, which combines both FFT and DMD, revealed that the formation mechanisms of pressure fluctuations at different frequencies are different. In particular, the pressure fluctuation at $4f_n$ in diffuser were caused by rotor–stator interaction (RSI) and flow separation near the suction surface (SS) of diffuser blades. Moreover, the pressure fluctuation at $2f_n$ was caused by flow separation near the SS of diffuser blades and wake vortex shedding. In impeller, the pressure fluctuations at $11f_n$ and $4f_n$ resulted from RSI and flow separation at the leading edge (LE) of impeller blades, respectively.

Article History

Received July 4, 2024
Revised December 11, 2024
Accepted December 22, 2024
Available online March 4, 2025

Keywords:

Axial flow pump
Pressure fluctuation
Dynamic mode decomposition
Numerical simulation
Rotor–stator interaction

1. INTRODUCTION

As fluid transport and boosting devices, axial flow pumps are widely employed in various fields, including petroleum and chemical industries, medicine and nuclear energy (Wang et al., 2007; Chen et al., 2016). Flow separation, vortices and pressure fluctuations often occur in axial flow pumps during operation due to their rotor–stator interaction (RSI) and complex channel structure, resulting in vibration, noise and potential structural damage (Zhang et al., 2017). Thus, studying pressure fluctuation characteristics and formation mechanisms of it has become a focal point in both industry and academia with the increasing request for operational stability, economy and safety in many industries.

RSI is generally believed to be the primary reason for pressure fluctuations in bladed pumps (Sano et al., 2019; Zhang et al., 2019). Dring et al. (1982) discovered that RSI primarily originates from wake and potential flow effects. Since then, many scholars have examined the features of pressure fluctuations and its main influencing factors in bladed pumps by experimental and numerical simulation methods. Experimentally, Shen et al. (2021) explored the effect of tip cavitation structures on pressure fluctuation in axial flow pumps by high-speed imaging and transient pressure measuring. Moreover, using dynamic pressure experiments, Dai et al. (2021) investigated the pressure fluctuation features of axial flow pumps during stalled operations, and they found that pressure fluctuations are influenced by blade passing, rotational and wake vortex shedding frequencies. Numerical calculation methods have recently gained significant attention with regard to obtaining information on entire flow fields, especially within rotating components. Zhang et al. (2018) implemented a numerical study on the interrelation between

NOMENCLATURE

f_n	rotating frequency of impeller	n	rotational speed
Q_d	rated flow rate	H_d	head
HL	axial length of impeller	DL	axial length of diffuser
δD	tip clearance	Δt	time step between snapshots
f	frequency	A_p	amplitude of pressure fluctuation
P	pressure	σ	growth rate of modes

pressure fluctuation and vortex in pump and found that tip leakage flow can cause vortices on the SS of the leading edge of blades, increasing pressure fluctuations. Kan et al. (2018) numerically explored pressure fluctuation in axial flow pumps during stalled operations, and they indicated that the primary source of fluctuations near impeller outlets is the vortex structure of diffusers. Studies on pressure fluctuations in pumps usually focus on the qualitative analysis of single flow field structures (Zhang et al., 2015; Lin et al., 2023), which result in mixed time–frequency information from flow fields and affect the formation mechanism of pressure fluctuation.

Given the distinct frequency characteristics of rotating machinery, analyses performed on coherent structures at specific frequencies have gained significant attention (Li et al., 2019). With the recent advancements in data reduction and decoupling methods, dynamic mode decomposition (DMD) (Schmid, 2010) has become a popular tool for analysing multivariate coupled information in complex flow fields. For instance, it can break down time data into distinct modes and extract vortex structure information that only contains specific frequencies, thereby realising reduced-order reconstruction of time data (Hemati et al., 2014; Ma et al., 2017; Kou & Zhang 2019; Ping et al., 2021). DMD can describe the evolution of various variables over time at a dynamic level and also reveal the temporal-spatial features of variables at different frequencies when applied to flow fields in rotating machinery. Yu et al. (2022) decoupled and reconstructed a flow field using DMD, and they could accurately reproduce the evolution of a flow structure at dominant frequencies. Moreover, they found that pressure area modes in volutes are primarily caused by pressure fluctuations that result from wake effects propagating downstream and persisting over long distances. Liu et al. (2019) used DMD for the order reduction analysis of a gas–liquid flow in a pump, and it could reveal a radial non-uniformity as the main coherent structure of the flow. Han & Tan (2020) used DMD to rebuild the tip leakage vortex (TLV) of a mixed-flow pump, showing that the top four modes with the highest energy ratios correspond to the primary and harmonic frequencies of TVL evolution. Overall, DMD has been increasingly adopted in decoupling flow fields in turbo-machine, indicating that it can effectively extract flow field information at characteristic frequencies.

In this study, aiming at studying the formation mechanism of pressure fluctuations in axial flow pumps, DMD was adopted to decouple an unstable flow field in an axial flow pump and extract coherent structures of its field modes. Then, their temporal-spatial evolution characteristics were analysed to reveal the formation mechanism of pressure fluctuations at characteristic frequencies, providing data support for subsequent research on the structural optimization and flow control of axial flow pumps.

2. PHYSICAL MODEL AND NUMERICAL METHOD

2.1 Physical Model

Figure 1 demonstrates the model of the pump used in this study. It includes an impeller and a diffuser, which consist of 4 blades and 11 blades, respectively. Table 1 shows the pump's primary design and geometric parameters. It can be seen that the passages of the impeller and the diffuser are contractive and diffusive, respectively. This special design is to prevent phase separation under multiphase flow conditions. A hydraulic performance test was conducted on the pump at the Lab of Multiphase Flow & Heat Transfer in Beijing Institute of Technology, and Fig. 2 demonstrates the test bench system. It consists of a motor, an axial flow pump, a control system, a water supply system, pipes and valves. An electromagnetic flow meter (model: HX-EMF; accuracy: 0.5%) was positioned in the inlet pipe, and pressure sensors (model: HX-2088; accuracy: 0.5%) were installed in the inlet and outlet pipes. A synchronous data acquisition card (model: USB-4000-BNC) was used for data collection.

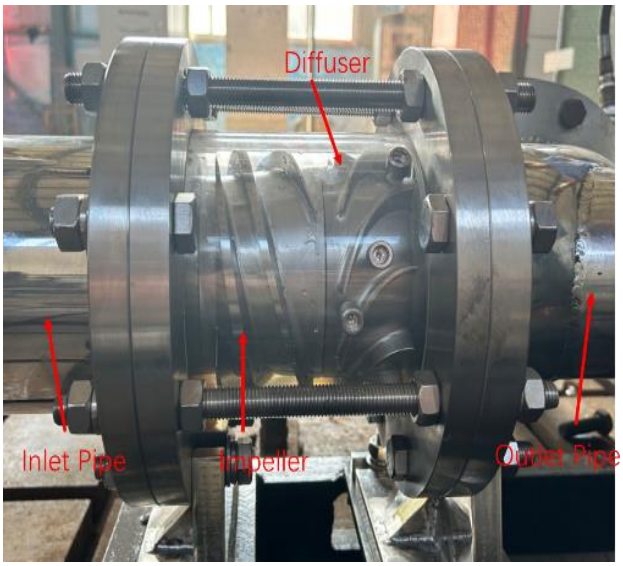

Fig. 1 Model of the experimental pump

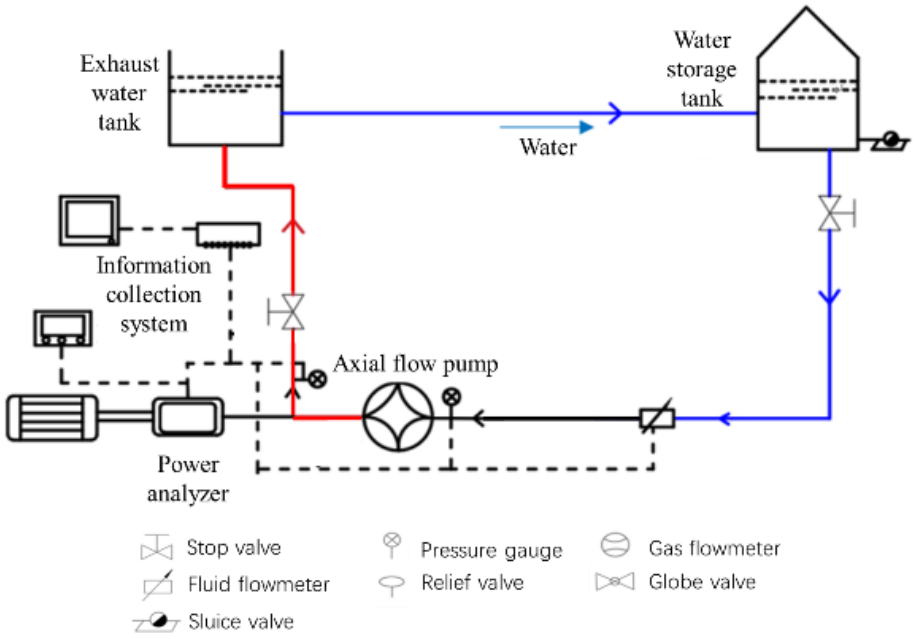

Fig. 2 Schematic diagram for testing the pump system

Table 1 Design and geometric specifications of the axial pump

Item	symbol	Value
rotational speed	n	2950 rpm
rated flow rate	Q	50 m^3/h
head	H	15 m
impeller blade number	Z_i	4
diffuser blade number	Z_d	11
axial length of impeller	HL	60 mm
axial length of diffuser	DL	40 mm
tip clearance	δD	0.4 mm
impeller inlet blade angle	β_1	8.5 deg
diffuser inlet blade angle	β_3	20 deg
pump shroud diameter	D_s	150 mm
impeller inlet hub diameter	D_{h1}	120 mm
impeller outlet hub diameter	D_{h2}	134 mm
diffuser inlet hub diameter	D_{h3}	134 mm
diffuser outlet hub diameter	D_{h4}	120 mm

2.2 Compute Domains and Grids

Reasonable boundary conditions were set, and the simulation domain was extended to include the inlet and outlet pipes, as demonstrated in Fig. 3. The monitoring points, R1–R4 and D1–D4, were sequentially named and streamwise distributed at 50% blade height in the pump, where R1–R4 are in the impeller passages and D1–D4 are in the diffuser passages, as shown in Fig. 4. The whole flow channel adopts a structural grid. For the inlet and outlet pipes, ICEM CFD 2022 R1 was used for mesh generation, while for the impeller and diffuser domains, TurboGrid 2022 R1 was employed instead. The mesh independence has already been validated (Li et al., 2021b). To balance accuracy with calculation efficiency, 3.68 million mesh elements were used. Furthermore, the grid information of the domains of the diffuser and impeller were extracted, as demonstrated in Table 2, confirming the satisfaction of criteria for the shear stress transport k-ω (SST k-ω) model.

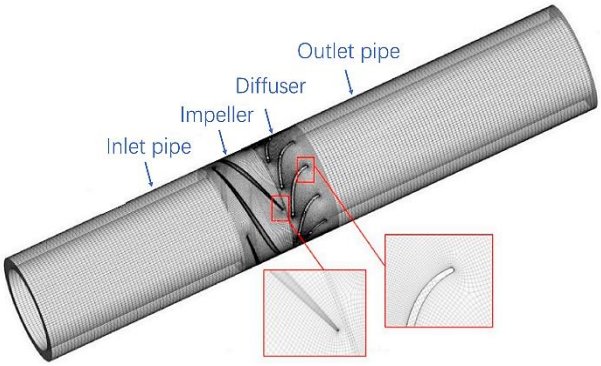

Fig. 3 Computation domain

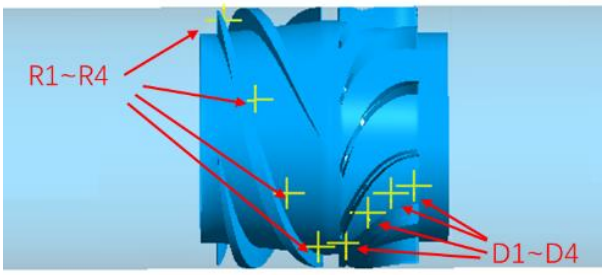

Fig. 4 Monitoring points

Table 2 Mesh information of the impeller and diffuser

	Impeller	Diffuser
number of elements	2,361,664	1,164,240
number of nodes	2,518,784	1,286,604
average y +	6.74	2.95
number of boundary layers	12	10
orthogonality	46-82	62-74
expansion factor	1.0-1.2	1.0-4.9

2.3 Numerical Methods

The internal flow was simulated using Ansys CFX 2022 R1, where the RANS equation was employed as a governing model. SST *k-ω* model was opted as a turbulence model, as it can effectively capture turbulent shear stress and provide correct predictions for flow separation under inverse pressure gradients in bladed pumps (Zhang et al., 2019; Wei et al., 2024). The inlet mass flow rate was specified as 13.85 kg·s^{-1}, while the outlet boundary situation was static pressure. The advective and turbulent numerical terms were discretised using a high-resolution format, while the transient terms were discretised using a second-order backward Euler format. The "transient rotor–stator method" was utilized to process data transmission at the rotor–stator interface.

The rotational speed (*n*) was 2950 rpm, and the time of the unstable flow was 1.13×10^{-4} s, which is consistent with an impeller rotation of 2°. The courant number was less than 1, and the total time was 0.2034 s, equating to 10 cycles of impeller rotation. The time step independence has already been validated (Zhang et al., 2019). The maximum iteration was 1500, and the convergence of the calculation was obtained when the RMS residual was less than 1×10^{-5}. The flow field data of the final four impeller rotation cycles were output for subsequent analyses. Based on the Nyquist sampling theorem (Nyquist, 1924), the frequency resolution was 12.33 Hz, and the maximum analysis frequency was 4425 Hz, which is 22.5 times of blade passing frequency (BPF). These values meet requirements of analysing frequency domain features of flow fields (Wei et al., 2022).

Fig. **5** demonstrates that the obtained head and efficiency values from the simulation and experiment were compared. The simulation consequences are in agreement with the experiment data at the same flow rate. In a design-based situation, the relative errors in efficiency and head are both within 5%, demonstrating the validity of the numerical method used in this research.

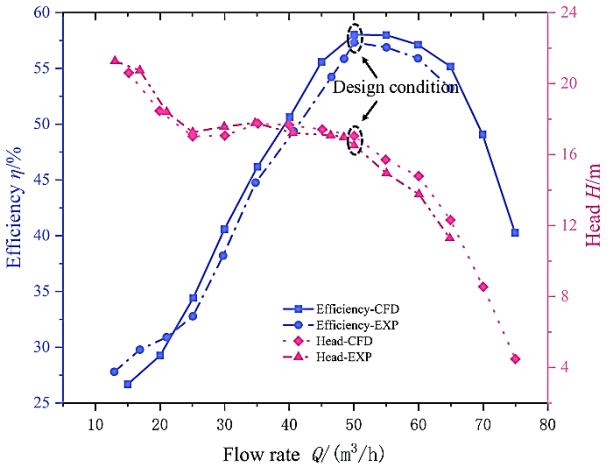

Fig. 5 Performance curves of efficiency and head based on the performed simulation and experiment

2.4 Dynamic Mode Decomposition Method

For nonlinear flows, DMD decouples flow field variables (e.g., velocity and pressure) and identifies dominant fluctuation frequencies and the spatial patterns of associated coherent structures. By analysing the contributions of different frequency modes, the dynamic characteristics and interactions of coherent structures can be revealed (Li et al., 2023). Given the distinct frequency features of flow in rotating machinery, DMD was used to decouple the coherent structures from the flow fields within pump.

Prior to utilizing the DMD method, the flow field data was prepared as vector form, represented as sequential snapshots with a consistent time step Δt between adjacent snapshots (Li et al., 2024). If ψi represents the flow field snapshot vector at time i, N indicates the number of snapshots. Thus, the matrix representing the flow variable from time 0 to N-1 can be expressed as follows:

$$\varphi_0 = [\psi_0, \psi_1, ..., \psi_{N-1}] \tag{1}$$

Since the time interval between adjacent snapshots is very small, it can be assumed that any two consecutive snapshots are related by a linear transformation as follows:

$$\psi_{n+1} = \mathrm{A}\psi_n \tag{2}$$

where the linear transformation matrix A translates the temporal-spatial flow field through Δt along time, representing the temporal change of the dynamic system. Accordingly, the matrix φ1 representing the flow fields from time 1 to N can be expressed using matrix φ_0 and A as follows:

$$\varphi_1 = [\psi_1, \psi_2, ..., \psi_N] = \mathrm{A}\varphi_0 \tag{3}$$

The eigenvectors and eigenvalues of matrix A represent DMD eigenvalues and modes, where the eigenvalues contain data on the frequencies and growth rates of the modes. Matrix A cannot be resolved in a straightforward manner; however, an appropriate matrix S can be gained from singular value decomposition (SVD) (Li et al., 2024), thereby providing information on the system's time variation.

Φ is the matrix containing the DMD modes ϕ_i, as shown in Fig. 6, and the matrix form for reconstructing the flow field with the first r-th modes is as follows:

$$[\psi_0\psi_1\cdots\psi_{N-1}] =$$
$$\Phi B\nu =$$
$$[\phi_1\phi_2\cdots\phi_r]\begin{pmatrix} a_1 & & & \\ & a_2 & & \\ & & \ddots & \\ & & & a_r \end{pmatrix}\times\begin{pmatrix} 1 & \mu_1 & \cdots & \mu_1^{N-1} \\ 1 & \mu_2 & \cdots & \mu_2^{N-1} \\ \vdots & \vdots & \ddots & \vdots \\ 1 & \mu_r & \cdots & \mu_r^{N-1} \end{pmatrix} \tag{4}$$

where B is a diagonal matrix. Each diagonal element αi represents the amplitude, indicating the contribution of the i-th mode to the initial flow field, and ν is the Vandermonde matrix formed by the eigenvalues μ_i of matrix A. The decomposed modes could display the coherent structures of the system and can thus rebuild the reduced-order form of complicated systems. It represents the temporal-spatial evolution of the flow field corresponding to the i-th mode when only the i-th term is present in each matrix on the right of Eq. (4).

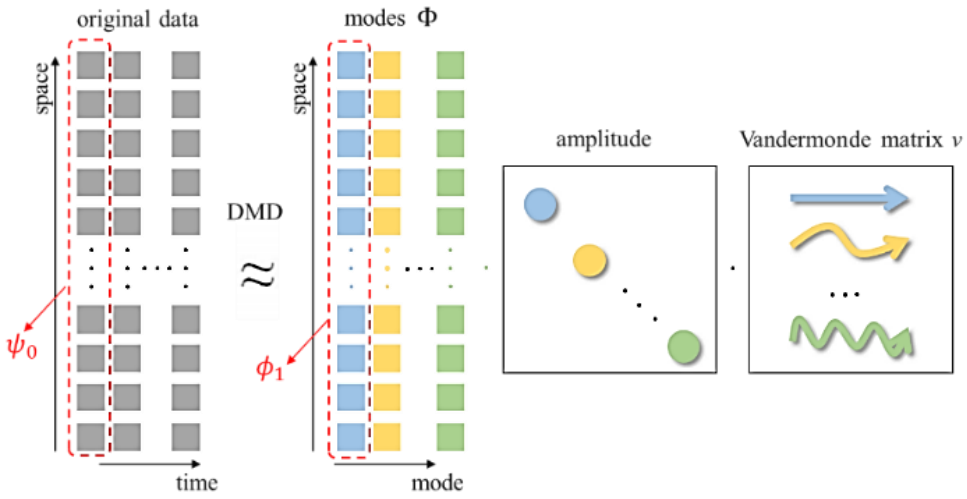

Fig. 6 Illustration of the DMD method

3. RESULTS AND DISCUSSION

3.1 Flow Field Analysis

Fig. **7** demonstrates the time-averaged allocation of pressure and velocity on the surface of span = 0.5, where the black crosses indicate the locations of the monitoring points R1–R4 and D1–D4. As shown in Fig. 7, the flow in the impeller was relatively stable, with a separation phenomenon happening at the LE of impeller blades resulting from the mismatch between the inflow angle and the blade angle. A local low-speed zone was formed at the trailing edge (TE) of impeller blades owing to backflow. The streamlines in the impeller were smooth, and there were no secondary flows and vortices. However, due to the diffusion characteristic, the pressure distribution in the diffuser passage was more complex, with local high-pressure zones present at the LE and the TE of the pressure surface (PS). Additionally, pressure distributions in all passages were similar. Flow separation occurred close to the SS of diffuser blades, forming two distinct vortices, i.e. Vortex 1 and Vortex 2, at the centre of the diffuser passage and the TE of diffuser blades, respectively. Moreover, the sizes and positions of the vortices in all passages were similar. Vortex 1 resulted from flow separation near the SS while Vortex 2 formed by the shedding of the wake vortex.

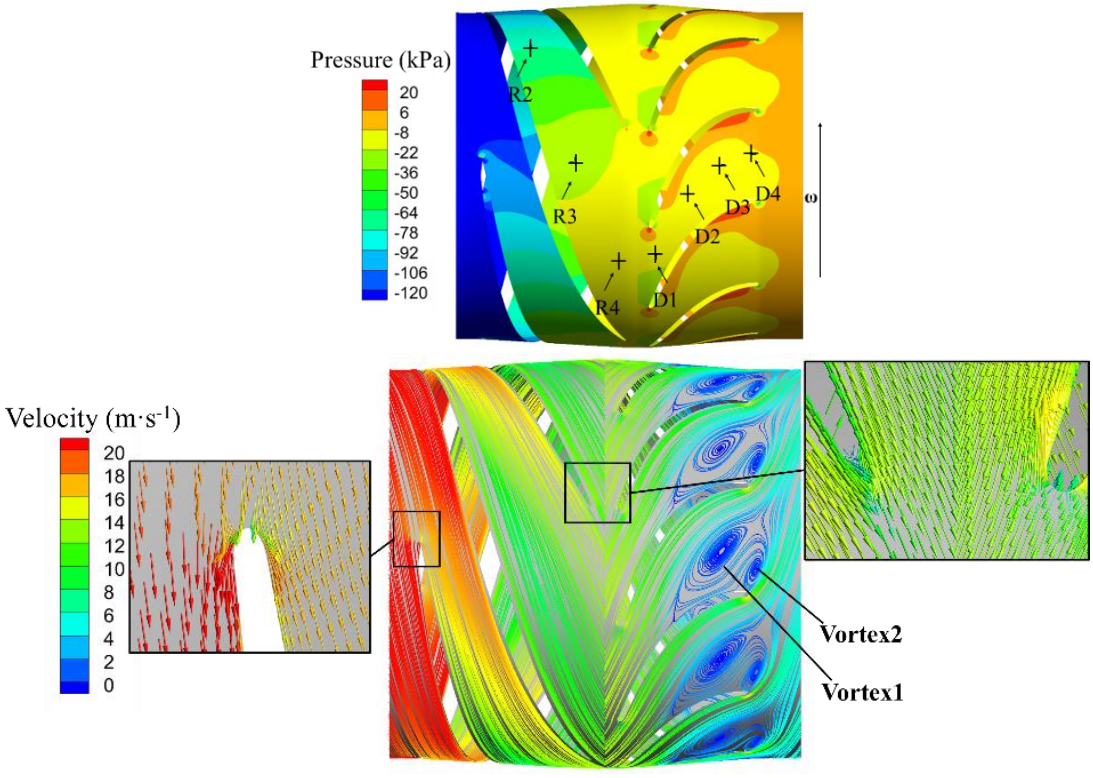

(a) Pressure (b) Velocity vector and streamline

Fig. 7 Time-averaged allocation of pressure and velocity on the surface of span = 0.5

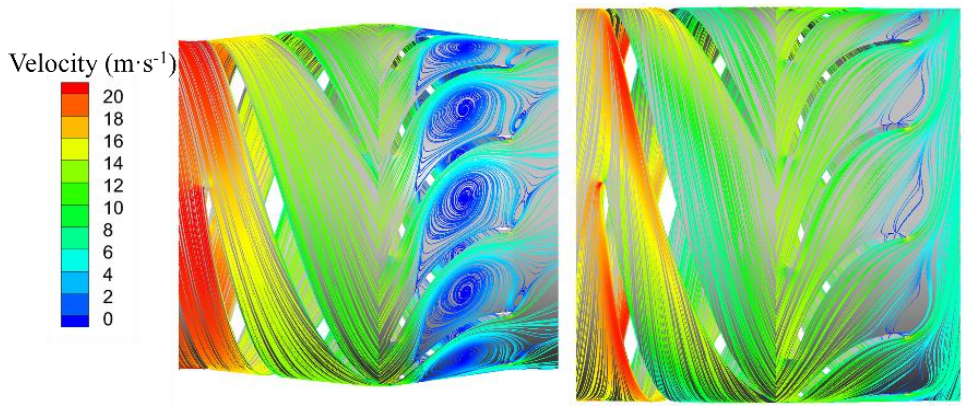

(a) span = 0.1 (b) span = 0.95

Fig. 8 Velocity on the surfaces of span = 0.1 and span = 0.95

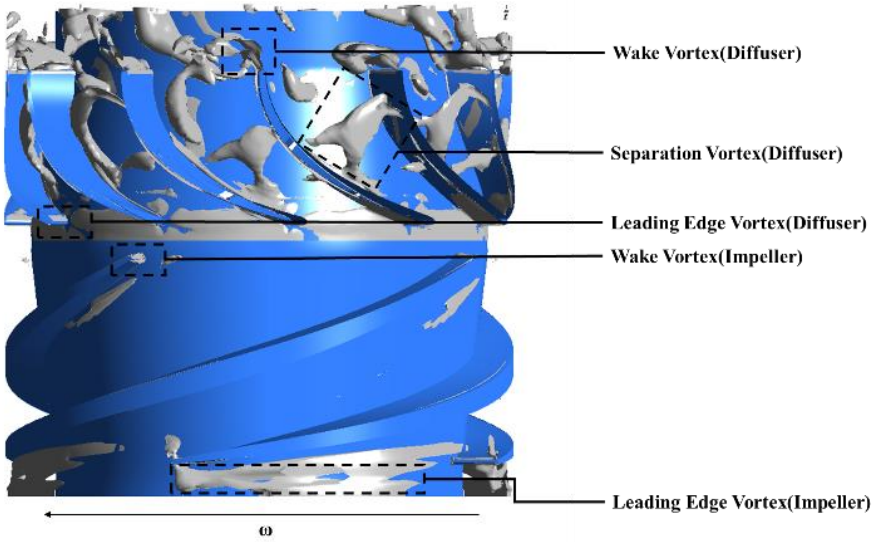

Fig. 9 Vortex distribution in the pump

Figure 8 demonstrates the time-averaged allocation of streamlines on the surfaces of span = 0.1 and span = 0.95. As demonstrated in Fig. 8, the flow in the impeller remains relatively stable. However, in the diffuser, the flow separation zone and vortex structures gradually grow from the tip to the hub. This is attributed to the unique design of the diffuser passage. Combined with the previous analysis about Vortex 1 and Vortex 2, it can be deduced that the flow near the tip is primarily influenced by wake vortex shedding, while the flow near the hub is mainly affected by flow separation. Meanwhile, on the surface of span = 0.5, both these two factors will play important roles.

Vortex structures have a significant effect on the internal flow field. Figure 9 shows the vortex structures visualized by the λ2 criterion, with a threshold of $-3.5\times10^{5}s^{-2}$ (Zhang et al., 2018) in the pump. It demonstrates that there were complex vortex structures in the pump. In the diffuser passage, there were mainly three types of vortexes: the leading-edge vortex resulting from the RSI, the separation vortex produced by flow separation and the wake vortex at the TE of the blade. In the impeller passage, a significant leading-edge vortex formed at the LE of the blade, gradually extending toward the LE of the adjacent blade in the opposite direction of rotation. Moreover, at the TE of the impeller blade, a small wake vortex was created by RSI.

3.2 Pressure Fluctuation Characteristics

After unsteady calculations, the pressure time features of all points could be obtained for one complete cycle, as shown in Fig. 10, which clearly shows that an obvious cyclical fluctuation occurred for the points. Within one impeller rotation cycle, there were 11 peaks and valleys for the points in the impeller and four peaks and valleys for the points in the diffuser. However, the amplitude of each peak varied.

The frequency features of the pressure fluctuation were studied, and the FFT approach was utilized to deal with the time–domain pressure data. Figure 11 demonstrates the frequency characteristics of pressure fluctuation at all points. The primary frequency and sub-fluctuation frequency are marked with red lines. Here, f_n is the shaft natural frequency, which is ~49 Hz. Under this

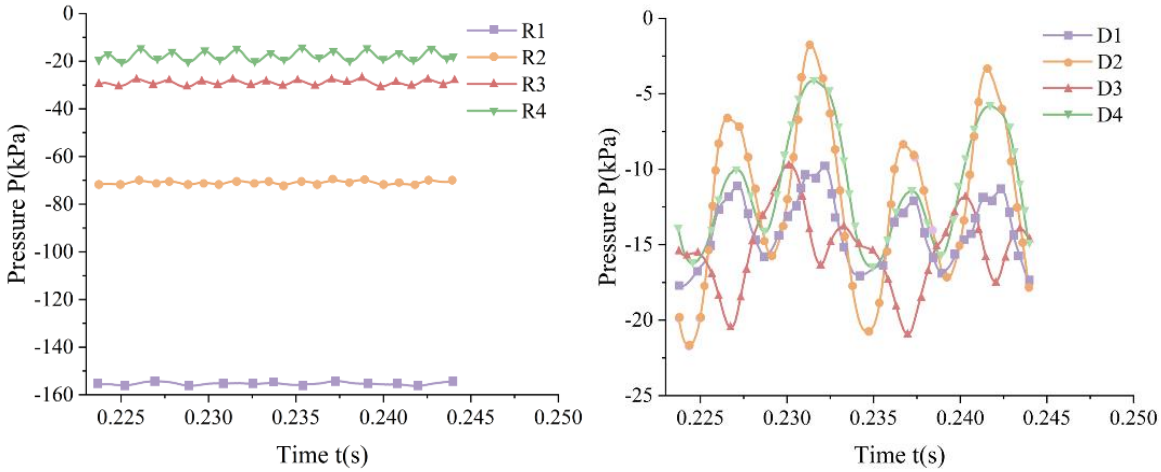

(a) Monitoring points R1–R4 (b) Monitoring points D1–D4

Fig. 10 Time domain characteristics of pressure fluctuation

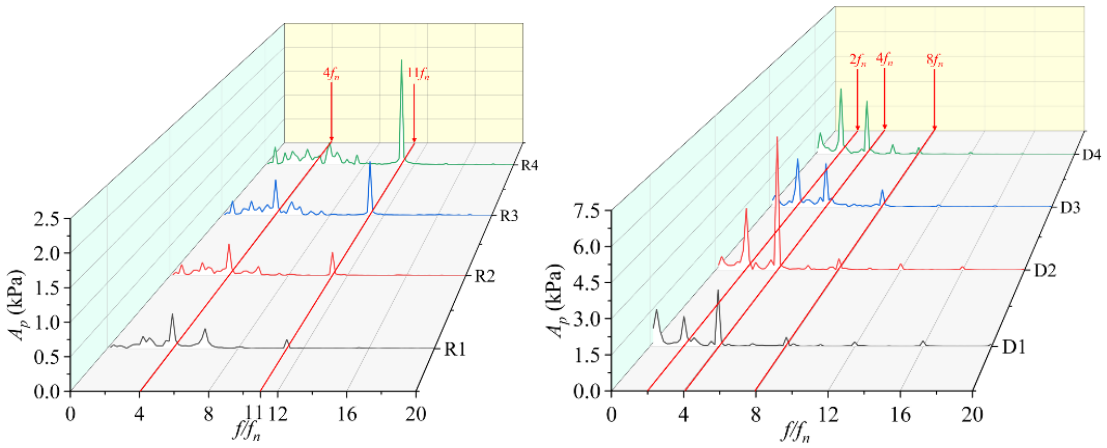

(a) Monitoring points R1–R4 (a) Monitoring points D1–D4

Fig. 11 Frequency domain characteristics of pressure fluctuation

operating condition, the dominant frequency at monitoring points in diffuser was $4f_n$, corresponding to the impeller BPF. Additionally, a pressure fluctuation peak was observed at $2f_n$. The dominant frequency at monitoring points in the impeller was $11f_n$, corresponding to the diffuser BPF. A significant peak also appeared at the impeller BPF. Overall, the pressure fluctuation amplitude at the points in diffuser was larger than that in impeller, with the largest amplitude observed at Point D2.

Based on the analyses above regarding the flows and pressure fluctuations in the pump, it can be concluded that there are complicated flow situations, including flow separation, backflow and vortices of various scales, with the pressure fluctuation peaks occurring at multiple frequencies. Thus, the flow field in the pump includes various forms and scales of coherent structures during its temporal-spatial evolution. However, the analysis above does not allow for decoupling and the identification of coherent structures across various frequencies (Zhang et al., 2022), making it hard to comprehend the mechanism of pressure fluctuation formation at the above-mentioned frequencies. Therefore, DMD was utilised in this research to analyse the unstable flows within the pump. See sections 3.3 and 3.4 for more details.

3.3 Mode Decomposition of Pressure Based on DMD

Transient flow field data under the design condition of 50 m³/h was selected for DMD as original data to decompose the pressure field and thus acquire the spatial allocation of the pressure modes. For easier calculations, three spanwise planes (span=0.1, span=0.5 and span=0.95) in the impeller and the diffuser were selected for data processing.

Generally, the shorter the time interval and the greater the number of snapshots, the higher the resolution and the smaller the inherent residuals of reconstructed flow fields (Liu et al., 2020). Thus, considering both computational efficiency and accuracy, the selected time interval was 0.000113 s, with a total number of 720 snapshots, resulting in 719 decomposable modes, with a unilateral spectrum width of 4424.78 Hz and a frequency resolution of 12.33 Hz.

Figure 12 illustrates the frequency–growth rate distribution with the colour indicating the lower and

higher energy modes, and the frequency–energy distributions of all modes on the three span sections. From the frequency–growth rate distribution, all modes have a corresponding mode with the same growth rate; however, the frequency was reversed. In DMD calculations, a negative frequency is a mathematical structure composed of complex exponential functions, with no direct physical interpretation (Li et al., 2023). All modal growth rates are less than or near 0, indicating that the pressure modes on each span section are stable modes with stable flow field structures. DMD captured the modes with frequencies identical to the frequency of the dominant pressure fluctuation, which has high energy and growth rates close to 0. These are considered the major modes of the flow field. The energy spectra on different span sections are similar to the pressure fluctuation spectra shown in Fig. 12. The difference is that pressure fluctuation fluctuations are specific to individual points, while DMD modes reflect energy distributions on entire span sections.

The frequency–energy distribution diagram indicates that the mode at frequency 0 contributes the highest energy of all modes, reflecting the fundamental steady-state characteristics of the unsteady flow field (defined as mode 0). The energy at different spans shows local peaks at $2f_n$, $4f_n$, $11f_n$ and their harmonic frequencies. A peak also appears at $6f_n$ on span = 0.95. However, as seen in Fig. 12(c2), this mode exhibits a relatively high absolute growth rate, indicating that it is a dissipative mode, which is generally considered a pseudo-mode caused by numerical calculation errors. This mode does not play a critical role in the rebuilding of flow fields (Li et al., 2023) and was thus not considered in this study. Considering the three factors of the local peaks, the dominant frequency of pressure fluctuations and the growth rate, modes 1, 2 and 3 were opted for further analysis, as demonstrated in Fig. 12. The frequencies corresponding to these three modes are 196Hz ($4f_n$), 98Hz ($2f_n$) and 540Hz ($11f_n$), respectively.

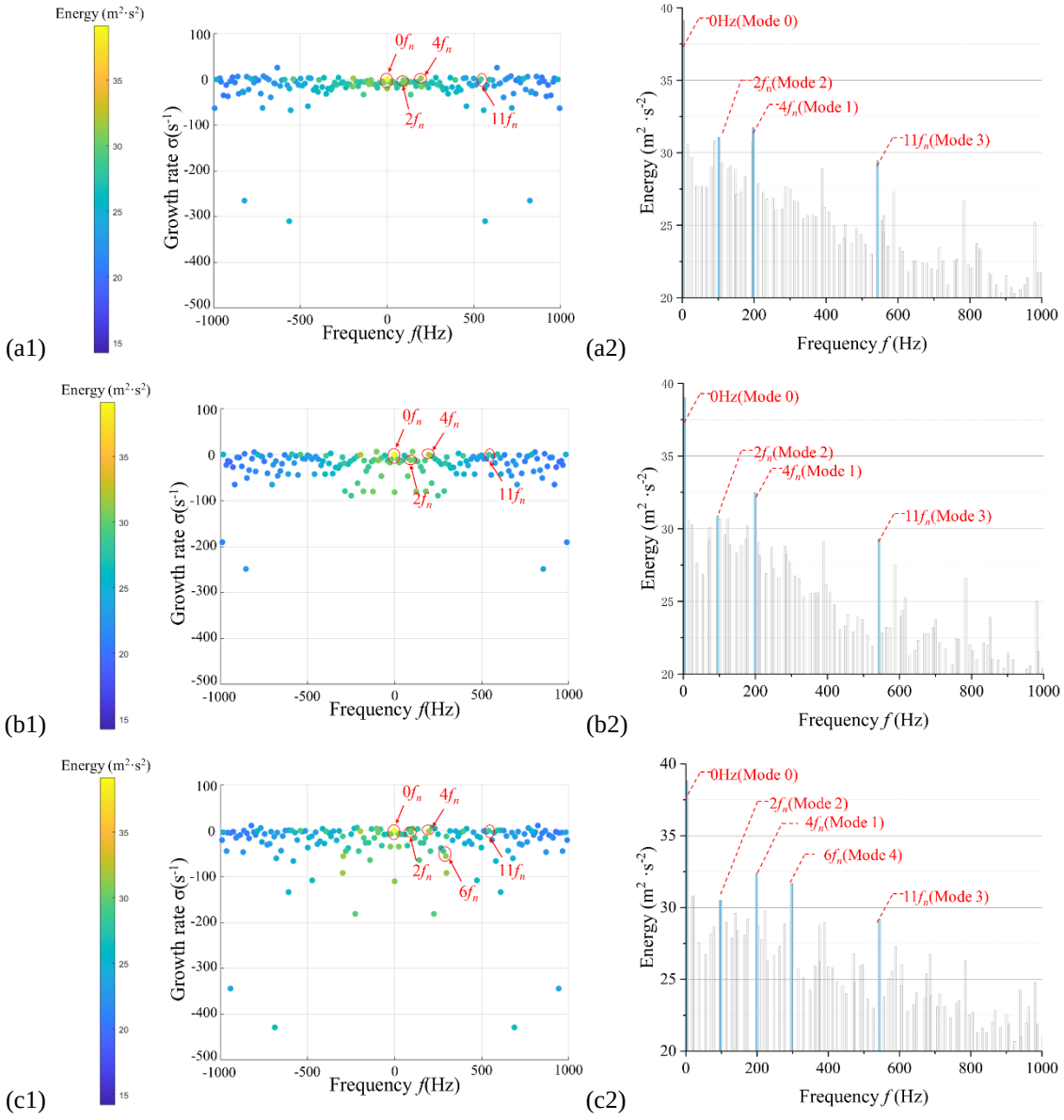

Fig. 12 Distribution of the frequency–growth rate and frequency–energy of pressure modes (from a to c: span = 0.1, 0.5, 0.95)

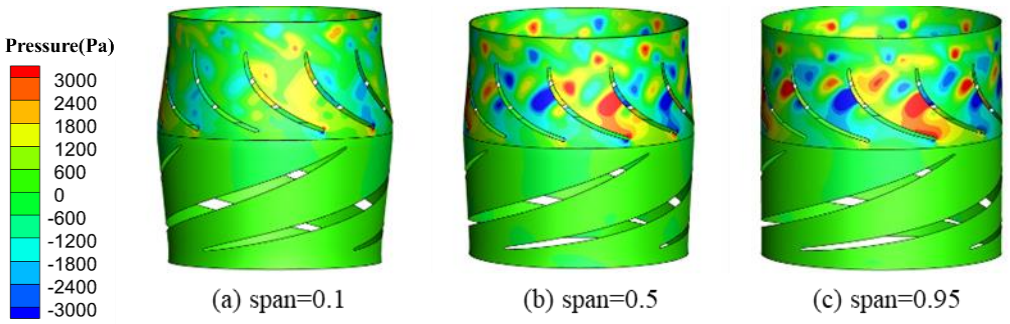

Fig. 13 Spatial allocation of DMD pressure modes at $4f_n$

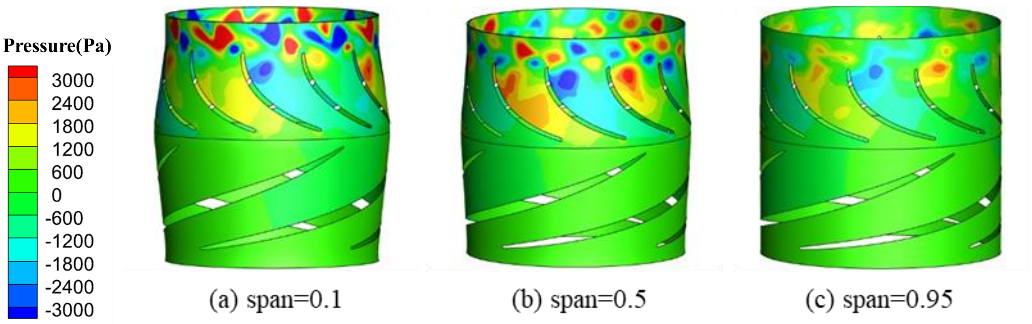

Fig. 14 Spatial allocation of DMD pressure modes at $2f_n$

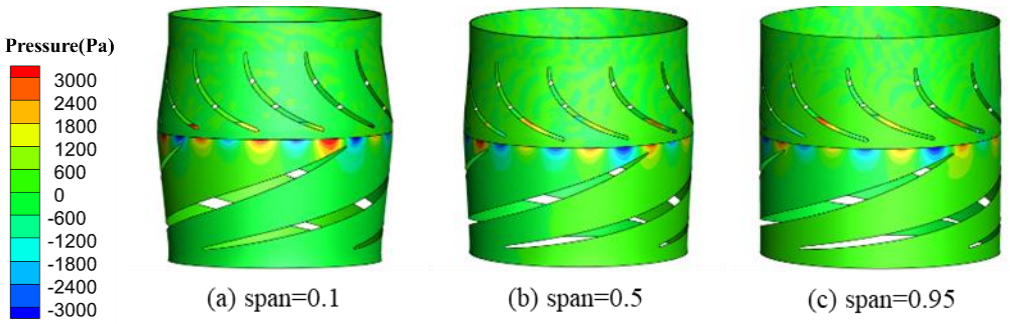

Fig. 15 Spatial allocation of DMD pressure modes at $11f_n$

Fig. **13**–Fig**. 15** show the spatial distribution of the pressure contours of modes 1–3 on three different span sections. The mode with the highest proportion of fluctuating energy on each section was Mode 1 ($f = 4f_n$). In this mode, large-scale high- and low-pressure zones appeared close to the SS of diffuser blade, with alternating zones of high- and low- pressure between adjacent channels. There were small amounts of high- and low-pressure zones distributed at the diffuser outlet. At the LE of diffuser blades, small and high-intensity high-pressure and low-pressure zones existed alternatively. For Mode 2 ($f = 2f_n$), high- and low- pressure zones were also distributed in the diffuser passage, with alternating distributions between adjacent passages but with different positions and intensities. In this mode, large-scale and high-intensity high- and low-pressure zones emerged close to the PS of diffuser blades, at the TE of blades and at the diffuser outlet. For Mode 3 ($f = 11f_n$), 11 pairs of periodic high- and low- pressure zones appeared in RSI region, interfering with the TE of impeller blades and resulting in great pressure fluctuations on the PS of impeller blades.

3.4 Formation Mechanism of Pressure Fluctuation

To further investigate the formation mechanism of pressure fluctuations at various dominant frequencies, the unsteady evolution process of pressure modes 1–3 was reconstructed according to Eq. (4). The analysis demonstrated in Fig. 12 indicates that the energy proportion of corresponding modes was analogous on different sections. By combining Fig. 13 and Fig. 15, similar flow patterns became evident across different sections for the same modes. Therefore, the section with span = 0.5 was analysed below.

3.4.1 Formation Mechanism in the Diffuser

The modal energy spectrum shown in Fig. 12 indicates that the pressure fluctuations at frequencies $4f_n$ and $2f_n$ have the highest energy proportion on each section, dominating and significantly impacting the flow field

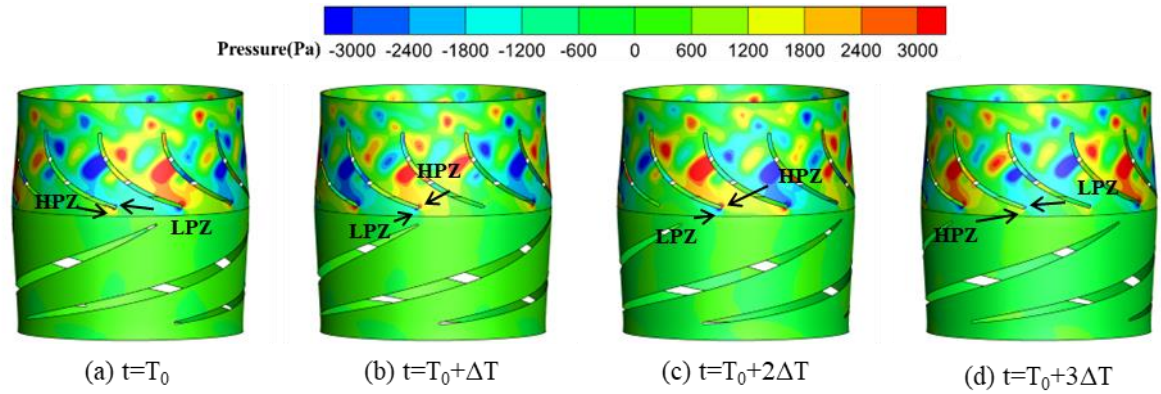

Fig. 16 Pressure distribution variation with time in Mode 1 (span=0.5, T_0=0.14238s, $\Delta T=1.13\times10^{-3}$s, high-pressure zone [HPZ], low-pressure zone [LPZ])

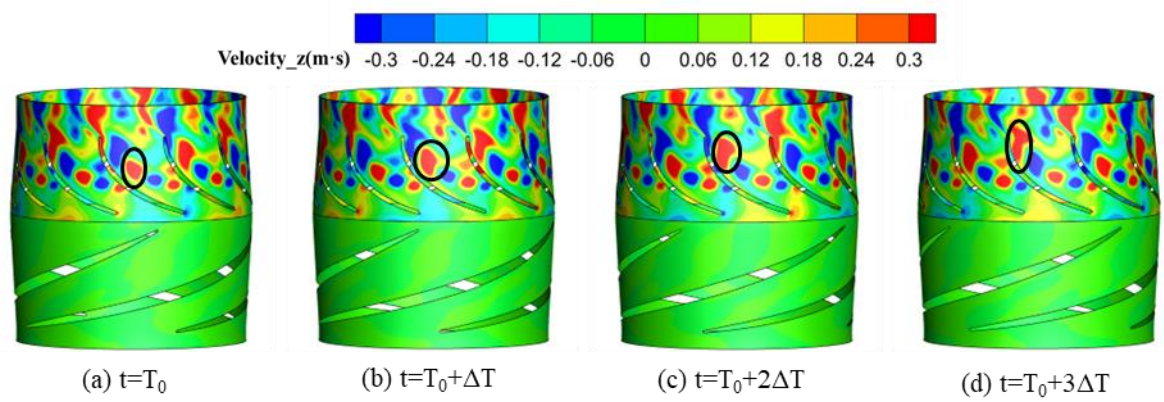

Fig. 17 Variation of axial velocity distribution with time in Mode 1 (span=0.5, T_0=0.14238s, $\Delta T=1.13\times10^{-3}$s)

inside the pump. By combining Fig. 13 and Fig. 14, it is apparent that the pressure fluctuations in modes corresponding to these two frequencies mainly occur in the diffuser passage. Therefore, the formation mechanism of the pressure fluctuations in the diffuser was first analysed.

Figure 16 and Fig. 17 illustrate the pressure variations and the axial velocity distribution with time in Mode 1 ($f = 4f_n$). Figure 16 shows that a pair of pressure fluctuation zones arose at the LE of the diffuser blade, one close to impeller passage and the other close to diffuser passage. With rotation of the impeller, the positive and negative values were alternated. In the diffuser, a local pressure fluctuation zone appeared near the SS of blades, connecting to the fluctuation zone at the LE of diffuser blades, with the same positive and negative values. Figure 17 shows that, due to the RSI effect, alternating high- and low-velocity zones arose at the LE of the diffuser blade (corresponding to the clockwise and counter-clockwise rotating vortices). These then entered the diffuser passage, moved downstream along the SS of the blade and shed at the middle of the SS of blades. Figure 7 shows that flow separation occurred at the corresponding position, generating Vortex 1. After shedding, it continued to move downstream, gradually approaching the PS and finally interfering with the solid wall of the TE of blades. In summary, pressure fluctuations in Mode 1 were mainly influenced by RSI and flow separation (Ni et al., 2017).

Figure 18 shows the spatial distribution of pressure with time in Mode 2. Unlike in Mode 1, the pressure fluctuation zone in Mode 2 appeared closer to the PS of diffuser blades. Additionally, there was a pressure fluctuation zone at the TE of diffuser blades (circled with solid black lines in Fig. 18). Figure 19 demonstrates the spatial allocation of the axial velocity mode at $2f_n$ with time. Similar to Mode 1, a series of high- and low-speed fluid masses (corresponding to vortices rotating in opposite directions) were generated due to flow separation at the front 1/3 chord length of the blade suction side, and they moved downstream along the flow channel (outlined with the dashed black line in Fig. 19). The vortex movement significantly impacted the local pressure distribution. Additionally, vortices were continuously generated and shed at the TE of diffuser blades (circled with solid black lines in Fig. 19), which is consistent with Vortex 2 in Fig. 7. Unlike in Mode 1, the speed fluctuation intensity of the high- and low-speed fluid masses in Mode 2 gradually increased along the flow and became maximum after shedding at the trailing edge, resulting in many high-intensity vortex structures distributed circumferentially at the diffuser outlet (circled with the grey line in Fig. 19). This result explains why the dominant frequency of the pressure fluctuation was $2f_n$ at Point D4, different with $4f_n$ at Point D2, as demonstrated in Fig. 11(b). In summary, the pressure fluctuation in Mode 2 is primarily attributed to the influences of flow separation and wake vortex shedding.

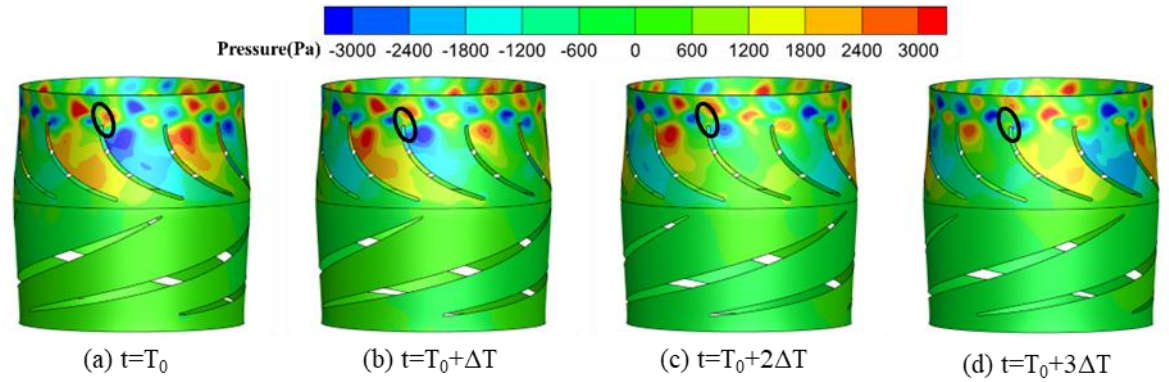

Fig. 18 Variation of pressure distribution with time in Mode 2 (span=0.5, T_0=0.14238s, $\Delta T=1.13\times10^{-3}$s)

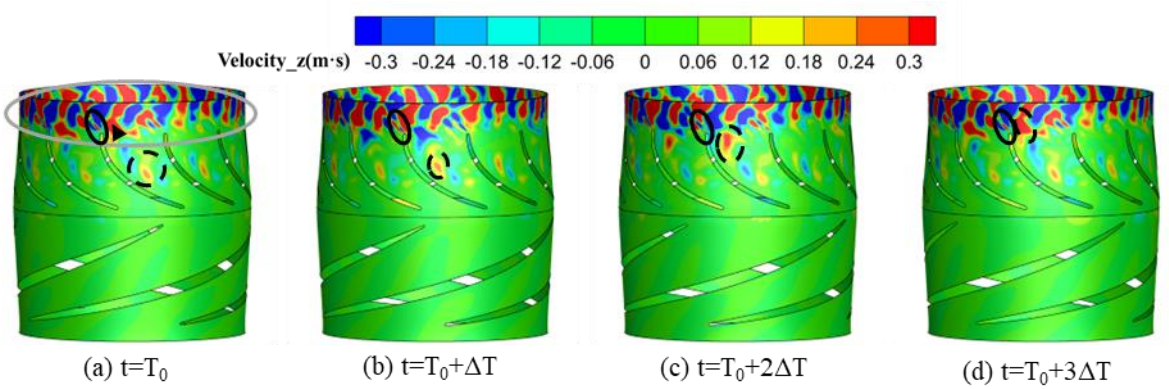

Fig. 19 Variation of axial velocity distribution with time in Mode 2 (span=0.5, T_0=0.14238s, $\Delta T=1.13\times10^{-3}$s)

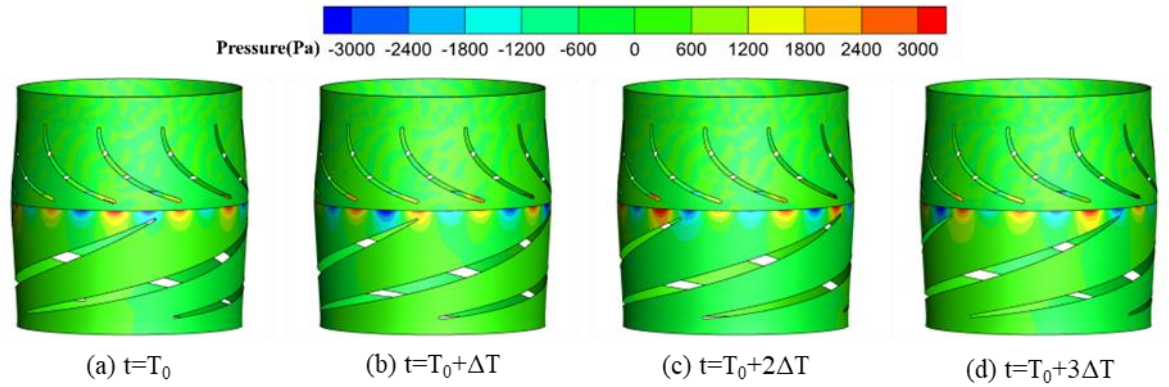

Fig. 20 Variation of pressure distribution with time in Mode 3 (span=0.5, T_0=0.14238s, $\Delta T=1.13\times10^{-3}$s)

3.4.2 Formation Mechanism in the Impeller

As demonstrated in Fig. 11(a), the dominant frequencies of pressure fluctuation at the monitoring points inside impeller were $4f_n$ and $11f_n$. The modes corresponding to these two frequencies were analysed separately.

First, an analysis was conducted on Mode 3, which has a larger energy proportion and corresponds to the frequency of $11f_n$. Figure 20 and Fig. 21 show the pressure variation and axial velocity distribution with time in Mode 3 ($f = 11f_n$). Figure 20 reveals that at this frequency, 11 pairs of high- and low- pressure zones appeared, with their positions relatively fixed with time, distributed on the side near the impeller in the RSI area, and their location corresponding to the position of the diffuser blades. The scale of the high- and low-pressure zones are smaller compared with Mode 1, only affecting the trailing edge region of the impeller blade. In combination analysis with Fig. 21, it can be seen that during the impeller rotation, periodic interactions occurred between the LE of diffuser blades and the TE of impeller blades, resulting in high- and low-speed zones and high- and low-pressure zones, thereby generating pressure fluctuations at $11f_n$ in the RSI region. Based on the DMD analysis, it could be concluded that the principal factor contributing to pressure fluctuations in Mode 3 is RSI.

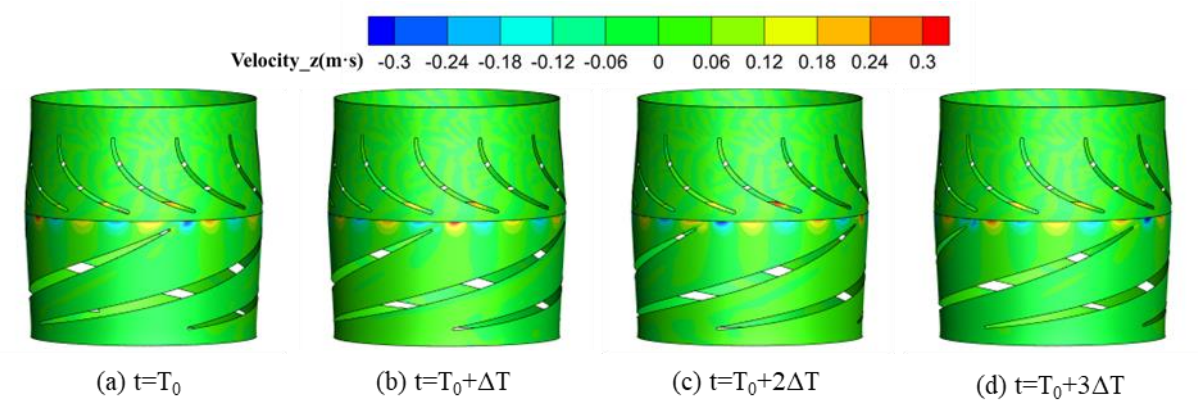

Fig. 21 Variation of axial velocity distribution with time in Mode 3 (span=0.5, T_0=0.14238s, $\Delta T=1.13\times10^{-3}$s)

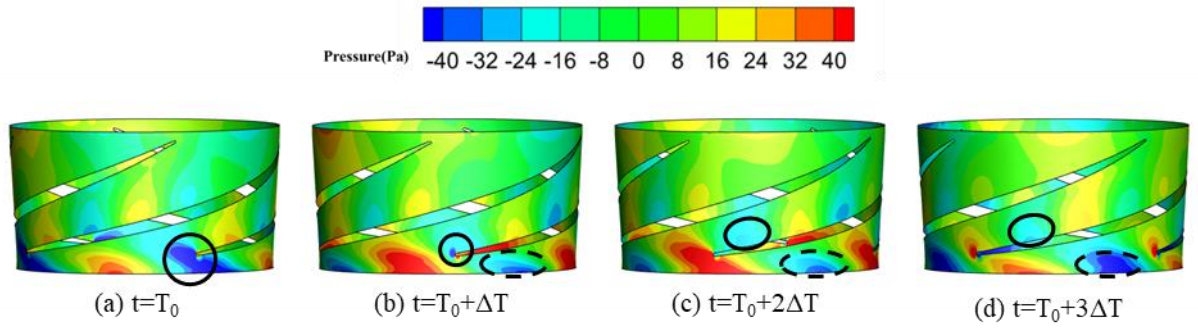

Fig. 22 Variation of pressure distribution with time in Mode 1 in the impeller (span=0.5, T_0=0.14238s, $\Delta T=1.13\times10^{-3}$s)

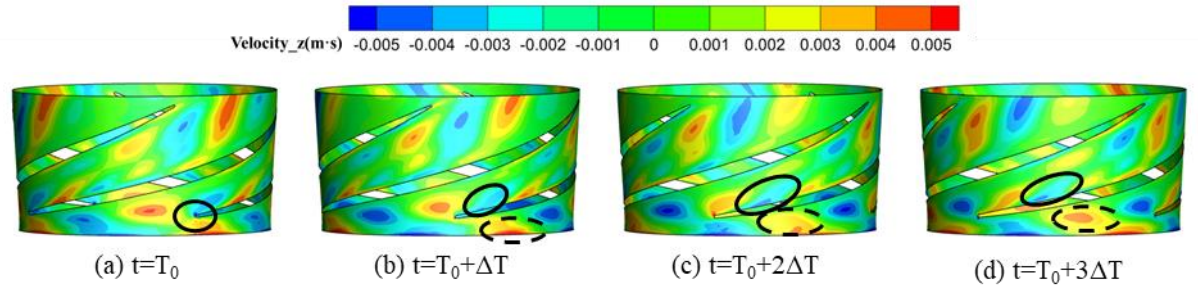

Fig. 23 Variation of axial velocity distribution with time in Mode 1 in the impeller (span=0.5, T_0=0.14238s, $\Delta T=1.13\times10^{-3}$s)

At the $4f_n$ frequency, the pressure fluctuation amplitudes inside the impeller were much smaller than that inside the diffuser, as shown in Fig. 11. Thus, the energy proportion was smaller, making it difficult to observe its coherent structure using Fig. 16. Then, the impeller passage was subjected to modal decomposition, and the mode of the $4f_n$ frequency was reconstructed to reveal the formation mechanism of pressure fluctuations at the $4f_n$ frequency in the impeller.

Figure 22 and Fig. 23 show the variations of pressure and axial velocity allocation with time in the impeller for Mode 1 ($f = 4f_n$), respectively. These figures also show that high- and low-pressure zones, as well as high- and low-velocity zones, were alternated at the LE of impeller blades, with their positions and scales changing over time. In combination with Fig. 7 and Fig. 9, it can be concluded that the coherent structures of the LE correspond to the separation vortices of the LE of impeller blades. Flow separation occurred at the LE of blades owing to the false match between the incident flow angle and blade setting angle. After being cut by the LE of blades, the incoming flow resulted in vortex structures close to the PS of impeller blades (circled by solid black lines, as shown in Fig. 22 and Fig. 23), which gradually moved downstream along the PS of blades, influencing the flow in impeller passage. The vortex structures close to the SS of the blades (circled by the dashed black lines in Fig. 22 and Fig. 23) moved in the opposite direction of rotation towards the adjacent blades, interfering with their LE and further affecting the generation of separation vortices at the LE of the adjacent blades. In conclusion, the pressure fluctuation

at $4f_n$ in impeller primarily resulted from the flow separation at the LE of blades.

4. CONCLUSION

In this study, the characteristics and formation mechanisms of pressure fluctuations inside an axial flow pump were studied using FFT and DMD, and the primary conclusions are summarized below:

1. Along the flow, the pressure fluctuation amplitude in impeller increased; however, it first increased and then decreased in diffuser, with the maximum amplitude occurring at the middle of diffuser passage. The amplitude of pressure fluctuations in diffuser was significantly higher than that in the impeller.
2. The frequency–energy and frequency–growth rate characteristics of each mode obtained using DMD aligned well with the pressure fluctuation spectrum, and DMD could identify the coherent structures of the pressure fluctuations at different frequencies. Moreover, analysing the flow field using DMD helped understand the formation mechanism of the pressure fluctuations at different frequencies within the axial flow pump.
3. In diffuser passage, the pressure fluctuations at $4f_n$ were affected by the RSI and flow separation close to the SS of diffuser blades; however, they were caused by flow separation near the SS and by wake vortex shedding at $2f_n$. In impeller passage, the pressure fluctuations were caused by RSI at $11f_n$; however, at $4f_n$, it was generated by flowing separation at the LE of impeller blades.

ACKNOWLEDGEMENTS

The article was supported by Hubei University of Automotive Technology PhD Foundation (BK202203) and the Beijing Municipal Natural Science Foundation (3212021).

CONFLICT OF INTEREST

The writers state that they were unaware of competing financial interests and individual relationships that may affect the work demonstrated in this article.

AUTHORS CONTRIBUTION

Ziyang Zhuang: Numerical investigation, data curation, programming, formal analysis and writing-original draft, writing-review & editing. **Huihui Zhou:** data curation, programming, and methodology. **Zhiyi Yu:** formal analysis, supervision, and writing-review.

REFERENCES

Chen, E., Ma, Z., Zhao, G., Li, G., Yang, A. & Nan, G. (2016). Numerical investigation on vibration and noise induced by unsteady flow in an axial-flow pump. *Journal of Mechanical Science and Technology*, *30*(12), 5397–5404. https://doi.org/10.1037/edu0000696

Dai, J., Liu, X., Huang, C., Xu, X., Bu, G., Zhong, Z., Xu F. & Dai, Q. (2021). Experiment on pressure fluctuation of axial flow pump system with different runaway head. *Processes*, *9*(1597), 1597. https://doi.org/10.3390/pr9091597

Dring, R. P., Joslyn, H. D., Hardin, L. W., & Wagner. J. H. (1982). Turbine rotor-stator interaction. *Journal of Engineering for Gas Turbines and Power*, *104*, 729-742. https://doi.org/10.1115/1.3227339

Han, Y., & Tan, L. (2020). Dynamic mode decomposition and reconstruction of tip leakage vortex in a mixed flow pump as turbine at pump mode. *Renewable Energy*, *155*(0), 725-734. https://doi.org/10.1016/j.renene.2020.03.142

Hemati, M. S., Williams, M. O., & Rowley, C. W. (2014). Dynamic mode decomposition for large and streaming datasets. *Physics of Fluids*, *26*(11). https://doi.org/10.1063/1.4901016

Kan, K., Zheng, Y., Chen, Y., Xie Z., Yang, G., & Yang, C. (2018). Numerical study on the internal flow characteristics of an axial-flow pump under stall conditions. *Journal of Mechanical Science and Technology*, *32*(10), 4683-4695. https://doi.org/10.1007/s12206-018-0916-z

Kou, J., & Zhang, W. (2019). Dynamic mode decomposition with exogenous input for data-driven modeling of unsteady flows. *Physics of Fluids*, *31*(5), 057106. https://doi.org/10.1063/1.5093507

Li, P., Dong, W., Jiang, H., & Zhang, H. (2024a). Analysis of axial force and pressure fluctuation of centrifugal pump as turbine impeller based on dynamic mode decomposition. *Physics of Fluids*, *36*(3), 1-11. https://doi.org/10.1063/5.0193869

Li, S., Li, F., Huang, Q., Pan, G., Wang, S., & Tian, X. (2023). On the space-time decomposition and reconstruction of the pump-jet propulsor flow field. *Ocean Engineering*, *286*(2), 115521. https://doi.org/10.1016/j.oceaneng.2023.115521

Li, W., Ji, L., Li, E., Shi, W., Agarwal, R., & Zhou, L. (2021). Numerical investigation of energy loss mechanism of mixed-flow pump under stall condition. *Renewable Energy*, *167*(11), 740-760. https://doi.org/10.1016/j.renene.2020.11.146

Li, W., Long, Y., Ji, L., Li, H., Li, S., Chen, Y., & Yang, Q. (2024). Effect of circumferential spokes on the rotating stall flow field of mixed-flow pump. *Energy*, 290, 130260. https://doi.org/10.1016/j.energy.2024.130260

Li, Y., He, C., & Li, J. (2019). Study on flow characteristics in volute of centrifugal pump based on dynamic mode decomposition. *Mathematical Problems in Engineering*, *2019*(1), 1-15. https://doi.org/10.1155/2019/2567659

Li, Y., Yu, Z., & Sun, W. (2021b). Drag coefficient

modification for turbulent gas-liquid two-phase flow in a rotodynamic pump. *Chemical Engineering Journal*, *417*(0), 128570. https://doi.org/10.1016/j.cej.2021.128570

Lin, Z., Yang, F., Ding, P., Teng, J., Yuan, Y., & Jin, Y. (2023). Analysis of pressure fluctuation and energy characteristics of guide vane for axial flow pump based on Hilbert–Huang transform considering impeller–guide vane interaction. *Science Progress*, *106*(3), 00368504231188627. https://doi.org/10.1177/00368504231188627

Liu, M., Tan, L., & Cao, S. (2019). Dynamic mode decomposition of gas-liquid flow in a rotodynamic multiphase pump. *Renewable Energy*, *139*(0), 1159-1175. https://doi.org/10.1016/j.renene.2019.03.015

Liu, M., Tan, L., & Cao, S. (2020). Method of dynamic mode decomposition and reconstruction with application to a three-stage multiphase pump. *Energy*, *208*(0), 118343. https://doi.org/10.1016/j.energy.2020.118343

Ma, X., Geisler, R., & Schröder, A. (2017). Experimental investigation of three-dimensional vortex structures downstream of vortex generators over a backward-facing step. *Flow, Turbulence and Combustion*, *98*(2), 389-415. https://doi.org/10.1007/s10494-016-9768-8

Ni, D., Yang, M., Gao, B., Zhang, N., & Li, Z. (2017). Numerical study on the effect of the diffuser blade trailing edge profile on flow instability in a nuclear reactor coolant pump. *Nuclear Engineering and Design*, *322*(0), 92-103. https://doi.org/10.1016/j.nucengdes.2017.06.042

Nyquist, H. (1924). Certain factors affecting telegraph speed. *Transactions of the American Institute of Electrical Engineers*, *3*(2), 324-346. https://doi.org/10.1002/j.1538-7305.1924.tb01361.x

Ping, H., Zhu, H., Zhang, K., Zhou, D., Bao, Y., Xu, Y., & Han, Z. (2021). Dynamic mode decomposition based analysis of flow past a transversely oscillating cylinder. *Physics of Fluids*, *33*(3), 1-16. https://doi.org/10.1063/5.0042391

Sano, T., Wakai, T., Reclari, M., Xu, Y., & Cao, S. (2019). *Investigation of internal flow pattern of a multiphase axial pump*. IOP Conference Series: Earth and Environmental Science. IOP Publishing, 240(6): 062058. https://doi.org/10.1088/1755-1315/240/6/062058

Schmid, P. J. (2010). Dynamic mode decomposition of numerical and experimental data. *Journal of fluid mechanics*, *656*(0), 5-28. https://doi.org/10.1017/S0022112010001217

Shen, X., Zhang, D., Xu, B., Shi, W., & B.P.M. van Esch. (2021). Experimental and numerical investigation on the effect of tip leakage vortex induced cavitating flow on pressure fluctuation in an axial flow pump. *Renewable Energy*, *163*, 1195-1209. https://doi.org/10.1016/j.renene.2020.09.004

Wei, A., Wang, S., Gao, X., Qiu, L., Yu, L., & Zhang, X. (2022). Investigation of unsteady cryogenic cavitating flow and induced noise around a three-dimensional hydrofoil. *Physics Fluids*, *34*(4), 042120. https://doi.org/10.1063/5.0088092

Wei, A., Wang, W., Hu, Y., Feng, S., Qiu, L., Zhang, X. (2024). Numerical and experimental analysis of the cavitation and flow characteristics in liquid nitrogen submersible pump. *Physics of Fluids*, *36*(4), 042109. https://doi.org/10.1063/5.0201907

Wang, F., Zhang, L., & Zhang, Z. (2007). Research on pressure fluctuation characteristics of unsteady flow field in axial flow pump. *Journal of Hydraulic Engineering*, *38*(8), 1003–1009. https://doi.org/10.1037/edu0000696

Yu, T., Shuai, Z., Wang, X., Jian, J., He, J., Meng, C., Dong, L., Liu, S., Li, W., & Jiang, C. (2022). Mechanism of the rotor− stator interaction in a centrifugal pump with guided vanes based on dynamic mode decomposition. *Physics of Fluids*, *34*(8), 087103. https://doi.org/10.1063/5.0098193

Zhang, D., Geng, L., Shi, W., *et al*. (2015). Experimental investigation on pressure fluctuation and vibration in axial-flow pump model. *Nongye Jixie Xuebao/Transactions of the Chinese Society of Agricultural Machinery*, *46*(6), 66-72. https://doi.org/10.6041/j.issn.1000-1298.2015.06.010

Zhang, J., & Tan, L. (2018). Energy performance and pressure fluctuation of a multiphase pump with different gas volume fractions. *Energies*, *11*(5), 1216. https://doi.org/10.3390/en11051216

Zhang, S., Chen, H., Ma, Z., Wang, D., & Ding, K. (2022). Unsteady flow and pressure fluctuation characteristics in centrifugal pump based on dynamic mode decomposition method. *Physics of Fluids*, *34*(11), 1-21. https://doi.org/10.1063/5.0097223

Zhang, W., Yu, Z., Li, Y., Yang, J., & Ye, Q. (2019). Numerical analysis of pressure fluctuation in a multiphase rotodynamic pump with air–water two-phase flow. *Oil & Gas Science and Technology–Revue d'IFP Energies nouvelles*, *74*(1), 18–30. https://doi.org/10.2516/ogst/2018101

Zhang, W., Zhu, B., Yu, Z., & Yang, C. (2017). Numerical study of pressure fluctuation in the whole flow passage of a low specific speed mixed-flow pump. *Advances in Mechanical Engineering*, *9*(5). https://doi.org/10.1177/1687814017707651

Zhang, Y., Liu, K., Xian, H., & Du, X. (2018). A review of methods for vortex identification in hydroturbines. *Renewable and Sustainable Energy Reviews*, *81*(1), 1269-1285. https://doi.org/10.1016/j.rser.2017.05.058